Applied Catalysis B: Environmental 342 (2024) 123451

Contents lists available at ScienceDirect

Applied Catalysis B: Environmental

journal homepage: www.elsevier.com/locate/apcatb

Tailoring the Mo-N/Mo-O configuration in MoO_2/Mo_2N heterostructure for ampere-level current density hydrogen production

Shuai Feng [a,1], Donglian Li [a,1], Hao Dong [a], Song Xie [a], Yaping Miao [b], Xuming Zhang [c], Biao Gao [c], Paul K. Chu [d], Xiang Peng [a,*]

[a] Hubei Key Laboratory of Plasma Chemistry and Advanced Materials, Engineering Research Center of Phosphorus Resources Development and Utilization of Ministry of Education, School of Materials Science and Engineering, Wuhan Institute of Technology, Wuhan 430205, China
[b] School of Textile Science and Engineering, Xi'an Polytechnic University, Xi'an 710048, China
[c] The State Key Laboratory of Refractories and Metallurgy, Institute of Advanced Materials and Nanotechnology, Wuhan University of Science and Technology, Wuhan 430081, China
[d] Department of Physics, Department of Materials Science and Engineering, and Department of Biomedical Engineering, City University of Hong Kong, Tat Chee Avenue, Kowloon, Hong Kong, SAR China

ARTICLE INFO

Keywords:
Hydrogen evolution reaction
Oxide-nitride heterostructure
Atomic configuration tailoring
Ampere-level current density hydrogen production
in situ phase separation

ABSTRACT

Mo-based electrocatalysts have garnered significant attention for their promising hydrogen evolution reaction (HER) efficiency, however, the strong adsorption of hydrogen poses a challenge to speedy gaseous hydrogen release. In this respect, regulating the coordination of Mo atoms is an efficient strategy to optimize the electronic configuration and accelerate the HER kinetics. Herein, MoO_2/Mo_2N heterostructures are prepared by a programmed *in situ* nitridation process. The precisely controlled Mo-N/Mo-O configuration in MoO_2/Mo_2N heterostructure weakens hydrogen adsorption on the Mo sites leading to HER with an ampere-level current density. The electrocatalyst delivers 1 A cm^{-2} at an overpotential of 335 mV in 0.5 M H_2SO_4. Furthermore, the electrocatalyst has excellent stability by maintaining a current density of 1 A cm^{-2} for 180 hours with a remarkable Faradaic efficiency of 99.8%. The results reveal a novel strategy to precisely modulate the electronic configurations of low-cost transition metal-based electrocatalysts boding well for industrial-scale hydrogen production.

1. Introduction

Owing to the renewable and environment-friendly properties, hydrogen has garnered broad attention as a promising alternative to fossil fuels [1–4]. In particular, hydrogen production by the hydrogen evolution reaction (HER) in electrochemical water splitting can be powered by sustainable energy sources to accomplish zero carbon emission [5,6]. However, efficient electrocatalysts are required for large current density HER in commercial electrochemical water splitting [7–11]. Wang et al. [7] have reported RuCo@$Ru_{SA}Co_{SA}$-NMC with a low overpotential of 255 mV for a current density of 1 A cm^{-2} and Zhang et al. [12] have constructed a robust self-supporting electrode of Ru-Ni $(OH)_2$ with excellent HER activity such as a current density of 2000 mA cm^{-2} at a small overpotential of 400 mV. Precious metals electrocatalysts are normally required to produce a large current density in HER, but their high cost and natural scarcity hinder wide commercial implementation, especially HER with ampere-level current densities. Hence, it is imperative to develop cost-effective and highly active non-noble metal-based electrocatalysts for industrial HER.

Mo-based compounds are promising HER electrocatalysts due to the abundant natural reserves and tunable configurations of the active sites [13,14]. In particular, molybdenum nitride (Mo_2N) is extensively studied for HER due to its distinctive electronic structure, high electrical conductivity, and mechanical stability [15,16]. However, the HER activity of Mo_2N is limited by the sluggish desorption of hydrogen because of the strong Mo-H bonding [17,18]. In this respect, regulating the electronic structure of the active sites can optimize the hydrogen adsorption characteristics and enhance the HER kinetics. Zhou et al. [19] have reported that the electronic interactions between the two phases in a heterostructure can be exploited to modify the hydrogen adsorption properties at the heterointerface to improve the HER efficiency. Fu et al. [20] have designed CoO-Mo_2N hollow heterojunctions

* Corresponding author.
E-mail address: xpeng@wit.edu.cn (X. Peng).
[1] These authors contributed equally to this work.

https://doi.org/10.1016/j.apcatb.2023.123451
Received 19 September 2023; Received in revised form 23 October 2023; Accepted 29 October 2023
Available online 2 November 2023

for effective HER based on the combined virtues of the hollow structure and heterojunctions. The CoO in CoO-Mo_2N facilitates the dissociation of water and the catalyst presents outstanding HER performance with an overpotential of 65 mV to afford the current density of 10 mA cm^{-2} in 1 M KOH. Previous works proved that combining the molybdenum nitride with oxides is beneficial to the optimized hydrogen adsorption properties and accelerated HER [21–23]. Considering that molybdenum dioxide (MoO_2) has low electrical resistivity and high stability, which has attracted much attention [24,25]. Constructing a heterostructure consisting of Mo_2N and MoO_2 with tailorable content and configuration would deliver favorable HER capability, which has seldom been reported and is challenging.

Herein, a coordination modulation strategy is designed and implemented to regulate the Mo-O/Mo-N configuration in the MoO_2/Mo_2N heterostructure obtained by *in situ* phase separation from MoO_3 nanowires. The amounts of Mo-O and Mo-N can be controlled precisely by a programmed nitridation process to produce superior HER properties with ampere-level current densities. For example, a high current density of 1 A cm^{-2} can be achieved at an overpotential of 335 mV in 0.5 M H_2SO_4 together with a Tafel slope of 88 mV dec^{-1}. In addition, the electrocatalyst works stably for 180 hours at a current density of 1 A cm^{-2}. Density-functional theory (DFT) calculations reveal that the MoO_2/Mo_2N heterostructure weakens H* absorption at the heterointerface, especially at Mo atoms of the Mo_2N phase, resulting in accelerated release of hydrogen from the active sites. The results provide insights into the modulation of active sites and the strategy has large potential in large current-density commercial hydrogen production.

2. Experimental details

2.1. Materials preparation

2.1.1. Synthesis of the MoO_3/CC precursor

Ammonium molybdate ($(NH_4)_2MoO_4$) (0.75 g) was dissolved in 10 mL of deionized water (DW) and heated to 70 °C for 30 min. Concentrated nitric acid (HNO_3) (40 mL) was added quickly to the solution under stirring and a piece of clean carbon cloth (CC) (2 × 3 cm^2) was immersed in the solution for 30 min. Afterwards, the CC was washed with DW several times to remove impurities. The product was denoted as MoO_3/CC.

2.1.2. Synthesis of the MoO_2/CC, MoON-x/CC, and Mo_2N/CC electrocatalysts

The MoO_3/CC precursor was annealed at 550, 600, and 650 °C for 2 h using a heating rate of 10 °C min^{-1} in a tube furnace under ammonia. The products were designated as MoON-1, MoON-2, and MoON-3, respectively. The pure Mo_2N/CC was synthesized by annealing the MoO_3/CC precursor at 700 °C for 2 h in NH_3 at a heating rate of 10 °C min^{-1}. The pure MoO_2/CC was prepared by annealing the MoO_3/CC precursor at 600 °C in N_2 for 2 h at a heating rate of 10 °C min^{-1}.

2.2. Materials characterization

The morphology of the samples was examined by scanning electron microscopy (FE-SEM, TESCAN MIRA4) and transmission electron microscopy (TEM, FEIF200) coupled with energy-dispersive X-ray spectroscopy (EDS). The composition and crystal structure were determined by high-resolution TEM (HR-TEM), and X-ray diffraction (XRD, LabX XRD-6100, Shimadzu) with a Cu K_α source. X-ray photoelectron spectroscopy (XPS, Thermo Scientific *K*-Alpha, Thermo Fisher) using monochromatic Al K_α X-ray was conducted to determine the chemical state of the samples.

2.3. Electrochemical measurements

The electrochemical measurements were carried out using a three-electrode configuration on the CHI 660E electrochemical workstation (Shanghai CH Instrument, China). The saturated calomel electrode (SCE) and graphite rod served as the reference electrode and counter electrode, respectively, and the electrocatalyst-modified CC was the working electrode. All the potentials were referenced to the reversible hydrogen electrode (RHE) according to Nernst equation $E_{RHE} = E_{SCE} + 0.242 + 0.059 \times pH$, where the pH of 0.5 M H_2SO_4 was measured to be 0.56 by a pH meter (FE28, Mettler Toledo). Linear sweep voltammetry (LSV) was conducted at a scanning rate of 10 mV s^{-1} with *iR*-compensation. The Tafel slope was calculated according to the formula $\eta = a + b\log(j)$ (η, overpotential; j, current density; a, constant; b, Tafel slope). Electrochemical impedance spectroscopy (EIS) was carried out at the initial potential of − 0.48 V *vs.* SCE in the frequency range of 100 kHz ~ 0.01 Hz with an amplitude of 5 mV. The electrochemically active surface area (ECSA) was determined by cyclic voltammetry (CV) at scanning rates of 15 ~ 40 mV s^{-1} in the potential window between − 0.05 and 0.05 V *vs.* SCE. The stability was determined at a constant current density of 1 A cm^{-2} and the amount of H_2 and O_2 produced was determined by the water displacement method.

2.4. Density-functional theory calculations

The DFT calculation was performed using the slab model with a vacuum space of 15 Å along the *z*-direction [26]. The exchange-correlation function under the generalized gradient approximation within the Perdew-Burke-Ernzerhof function was implemented. The Brillouin zone was sampled with 1 × 1 × 1 *k*-point mesh in all of the models. The convergence tolerances of the optimal configuration for the energy, force, and maximum displacement were 1.0 × 10^{-5} Ha, 0.002 Ha $Å^{-1}$, and 0.005 Å, respectively.

The Gibbs free energy for hydrogen adsorption (ΔG_{H^*}) was calculated as follows:

$$\Delta G_{H^*} = \Delta E_{H^*} + \Delta E_{ZPE} - T\Delta S \quad (1)$$

$$\Delta E_{H^*} = E_{(slab+H^*)} - E_{(slab)} - \frac{1}{2}E_{H_2} \quad (2)$$

where ΔE_{ZPE} stands for the change in the zero-point energy and ΔS is the entropy. Here, we used the value of 0.24 eV for $\Delta E_{ZPE} - T\Delta S$ according to Nørskov et al. [27].

3. Results and discussion

3.1. Morphology and composition of the electrocatalysts

Fig. 1**a** illustrates schematically the synthesis of the MoON electrocatalysts. The MoO_3 nanowire arrays are grown on the CC by a solution method in a hot bath with ammonium molybdate and nitric acid as the precursors. MoO_3 is then converted gradually into nitride by a programmed thermal treatment in an ammonia atmosphere. As a result, final products with different nitride concentrations are obtained. The tunable composition of Mo-O and Mo-N and subsequent interactions between these two phases modulate the electronic configurations of the Mo sites to enhance the electrocatalytic activity.

The FE-SEM images of MoO_3/CC in Fig. 1**b-c** reveal that the nanowire arrays (120–180 nm in diameter) cover the carbon fibers. After the thermal treatment in ammonia at 550 ~ 700 °C, no obvious morphological change can be observed from Figs. S1–2 and 1**d–e**. The diameter of the nanowires is 150–250 nm. After the thermal treatment of MoO_3 in N_2 at 600 °C (MoO_2/CC), the nanowire arrays on CC can also be observed in Fig. S3. XRD is performed to identify the phase and composition of the products. The diffraction peaks of the product obtained by the solution method can be indexed to MoO_3 (JCPDS card No. 21–0569), as shown in Fig. S4. After the thermal treatment in ammonia at 550 °C, the diffraction peaks at 37.4°, 43.5°, and 63.1° can be ascribed to Mo_2N (JCPDS card No. 25–1366), whereas those at 26.0°,

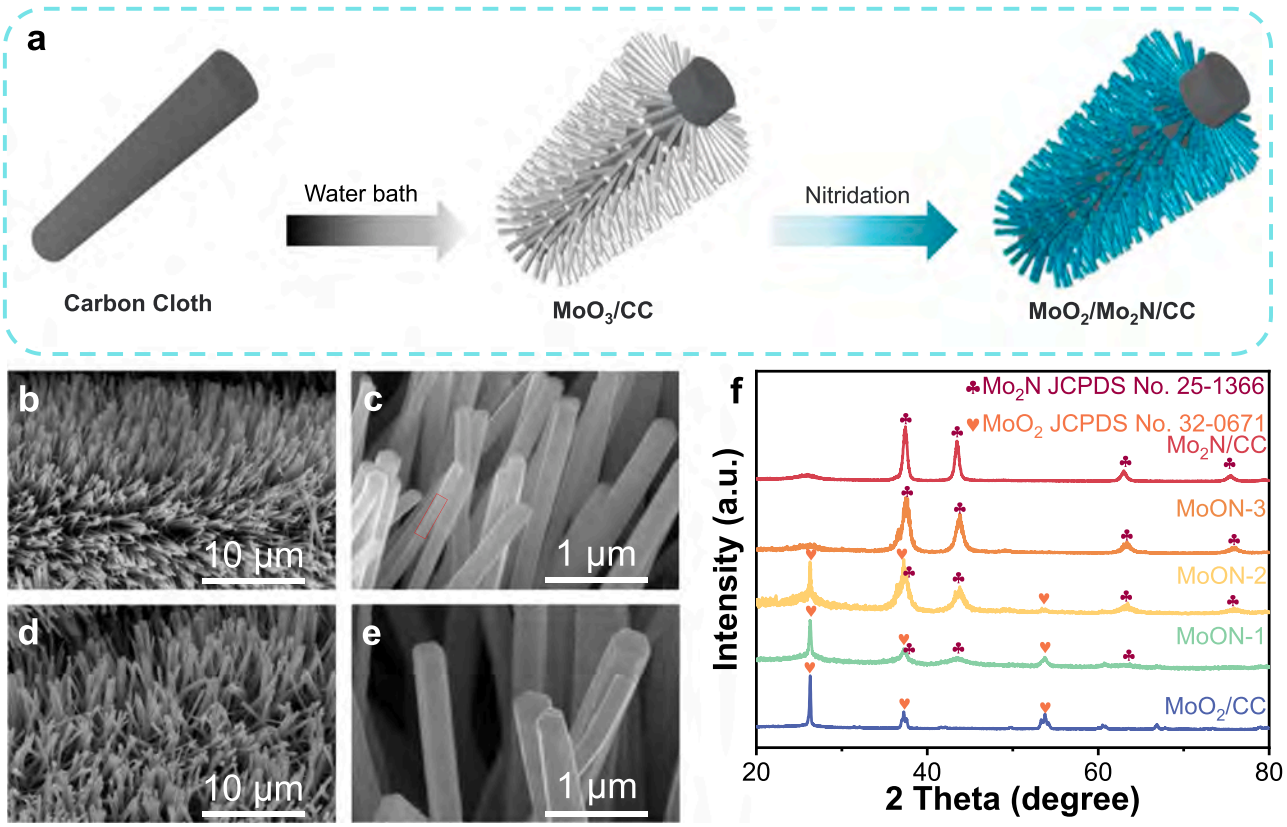

Fig. 1. (a) Schematic showing the fabrication of the MoON electrocatalysts; SEM images of (b-c) MoO_3 and (d-e) MoON-2; (f) XRD patterns of MoO_2/CC, MoON-1, MoON-2, MoON-3, and Mo_2N/CC.

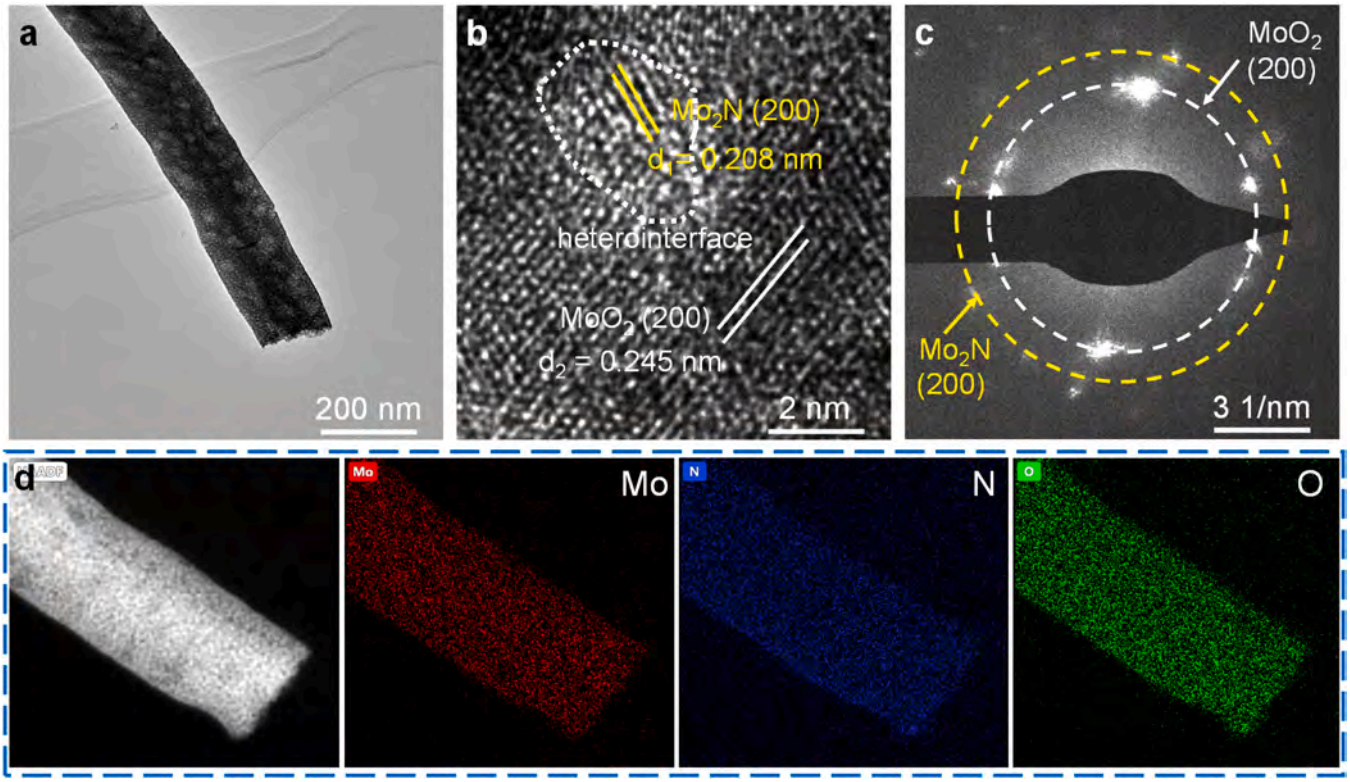

Fig. 2. (a) TEM image, (b) HR-TEM image with a dotted line showing the mismatch of the crystal planes, (c) SAED pattern, and (d) Elemental maps of Mo, N, and O in MoON-2.

37.0°, and 53.5° correspond to MoO_2 (JCPDS card No. 32–0671), suggesting that the product is a composite of Mo_2N and MoO_2, as indicated in Fig. 1**f**. By increasing the treatment temperature gradually from 550° to 700°C, the diffraction peaks from Mo_2N are enhanced, but those from MoO_2 weaken. When the temperature is 650 °C, only Mo_2N can be observed from Fig. 1**f** (red line), implying that MoO_3 has been converted into Mo_2N by the programmed thermal treatment in ammonia. It is noted that in this technique, the ratio of Mo-based oxide and nitride can be controlled. In addition, by annealing the MoO_3/CC at 600 °C for 2 h under N_2, the pure phase of MoO_2 (JCPDS card No. 32–0671) can be produced, as shown in Fig. 1**f** (blue line).

The TEM image in Fig. 2**a** reveals the nanowire morphology of MoON produced by the solution method and the following thermal treatment in ammonia, which is similar to the SEM image. The nanowire is 170 nm in diameter. The HR-TEM image in Fig. 2**b** shows lattice fringes of 0.245 and 0.208 nm arising from MoO_2 (200) (JCPDS card No. 32–0671) plane and Mo_2N (200) (JCPDS card No. 25–1366) plane, respectively. The mismatch of Mo_2N and MoO_2 planes can be observed, as labelled in Fig. 2**b**, indicating the generation of heterointerface during the *in-situ* phase separation protocol, consistent well with the previous works [28, 29]. There will be atomic interaction at the heterointerface to optimize the electronic structure of the surface sites for facilitated electrocatalysis [30–32]. Fig. 2**c** presents the selected area electron diffraction (SAED) image of MoON-2. The diffraction rings can be assigned to MoO_2 and Mo_2N matching the XRD and HR-TEM results. The EDS elemental maps of Mo, O, and N in Fig. 2**d** indicate homogeneous distributions of these elements.

The composition and chemical state of the electrocatalysts are determined by XPS. The survey spectra in Fig. 3**a-b** reveal the presence of Mo, O, and N elements in the samples thermally treated in ammonia. The high-resolution XPS Mo-3*d* spectra in Fig. 3**c** show two peaks at 236.1 and 232.8 eV stemming from Mo^{6+}-O from slightly surface oxidation [33]. The peaks at 230.0 and 233.1 eV correspond to the Mo-3$d_{5/2}$ and Mo-3$d_{3/2}$ of Mo^{4+}-O species in MoO_2 [28], and the other two peaks at 229.4 and 232.6 eV are associated with Mo-3$d_{5/2}$ and Mo-3$d_{3/2}$ of Mo-N in Mo_2N [34,35]. The high-resolution XPS N-1*s* spectrum (Fig. S5) of MoON-2 shows the N-Mo bond at 398.1 eV and Mo-3*p* at 395.4 eV [36,37].

To determine the surface composition of the electrocatalysts, the amounts of Mo-O and Mo-N species are calculated based on the integrated areas in the fitted Mo-3*d* spectra. Fig. 3**d** shows that with the increasing treatment temperature in ammonia, the concentration of Mo^{4+}-O species decreases from 69% in MoON-1–30% in MoON-3. At the same time, the concentration of Mo-N increases from 11% in MoON-1–50% in MoON-3. The signal of Mo^{4+}-O disappears when the temperature is increased to 700 °C, suggesting that the Mo-O species have been converted completely into Mo-N. The results also demonstrate that the amounts of Mo-O and Mo-N species can be modulated precisely by the programmed thermal treatment in ammonia. The *in situ* generated and precisely controlled Mo-N species interact strongly with the Mo-O host at the heterointerface. Hence, a well-designed Mo-O/Mo-N configuration at the heterointerface is expected to optimize hydrogen adsorption in HER for enhanced electrocatalytic efficiency.

3.2. Electrochemical properties

All the potentials were *iR* corrected unless otherwise specified to evaluate the intrinsically catalytic capability of the as-prepared electrocatalysts for HER. Fig. 4**a** shows the LSV curves of the Mo-based electrocatalysts in comparison with the bare CC and commercial Pt/C (20%) in 0.5 M H_2SO_4. MoON-2 requires an overpotential of 300 mV for a current density of 500 mA cm^{-2}, which is much smaller than those of MoON-1 (470 mV), MoON-3 (418 mV), Mo_2N (517 mV), MoO_2 (640 mV), MoO_3 (853 mV), and commercial Pt/C (492 mV). Notably, the current density of MoON-2 electrocatalyst can reach 1 A cm^{-2} at an overpotential of a mere 335 mV, which is distinctly smaller than that of the others. The LSV curves without *iR* compensation in Fig. S6 indicate the promising practical application of the MoON electrocatalyst. The Tafel slopes are obtained by fitting the linear regions of the Tafel plots. The Tafel slope of MoON-2 is 88 mV dec^{-1}, which is smaller than those of MoON-1 (134 mV dec^{-1}), MoON-3 (101 mV dec^{-1}), MoO_2 (153 mV dec^{-1}), MoO_3 (245 mV dec^{-1}), Mo_2N (110 mV dec^{-1}), CC (287 mV dec^{-1}) and close to that of commercial Pt/C (65 mV dec^{-1}), as indicated in Fig. 4**b**. The Tafel slope of MoON-2 suggests the Volmer-Heyrovsky mechanism and electrochemical desorption of hydrogen is the rate-determining step [38]. The smaller overpotential and Tafel slope suggest higher electrocatalytic activity and faster kinetics for MoON-2. Moreover, Fig. 4**c** shows that MoON-2 has a smaller charge transfer resistance (R_{ct}) of 8.5 Ω compared to MoON-1, MoON-3, Mo_2N, MoO_2, and commercial Pt/C thereby confirming the fast HER kinetics, which is promising for industrial-scale application.

The HER activity depends on the ECSA, which can be expressed by the electrochemical double-layer capacitance (C_{dl}) in the non-Faradic regions based on the cyclic voltammetry curves [39], as shown in

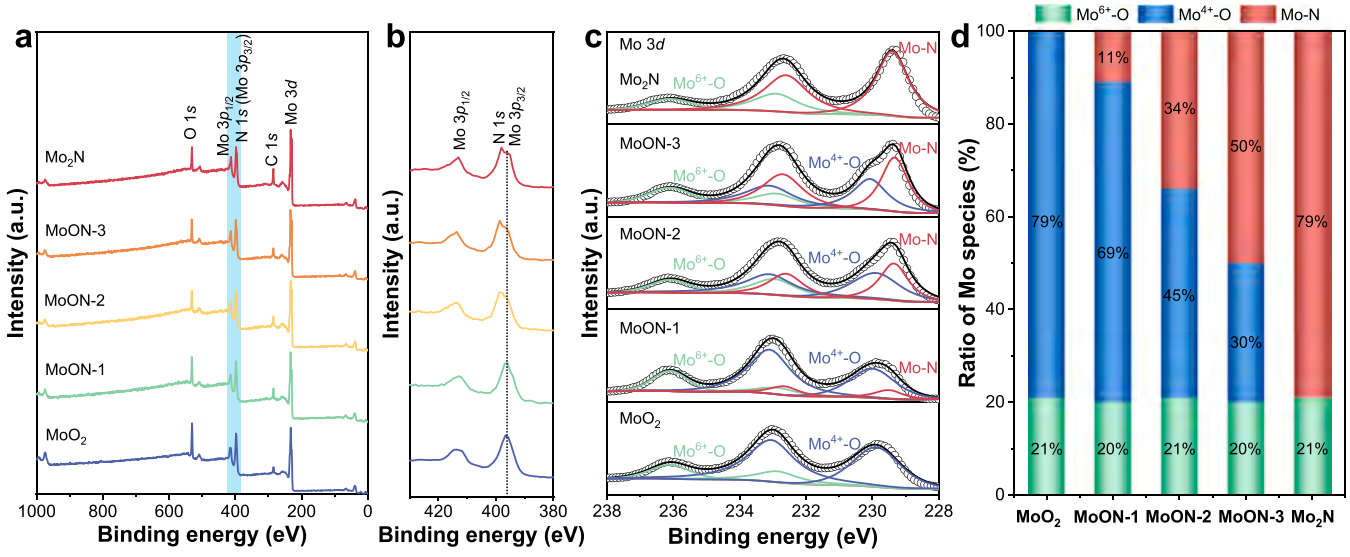

Fig. 3. XPS survey spectra of the electrocatalysts in the binding energy range of (a) 0 ~ 1000 eV and (b) 380 ~ 430 eV; (c) High-resolution XPS Mo-3*d* spectra; (d) Ratios of Mo species in MoO_2, MoON-1, MoON-2, MoON-3, and Mo_2N.

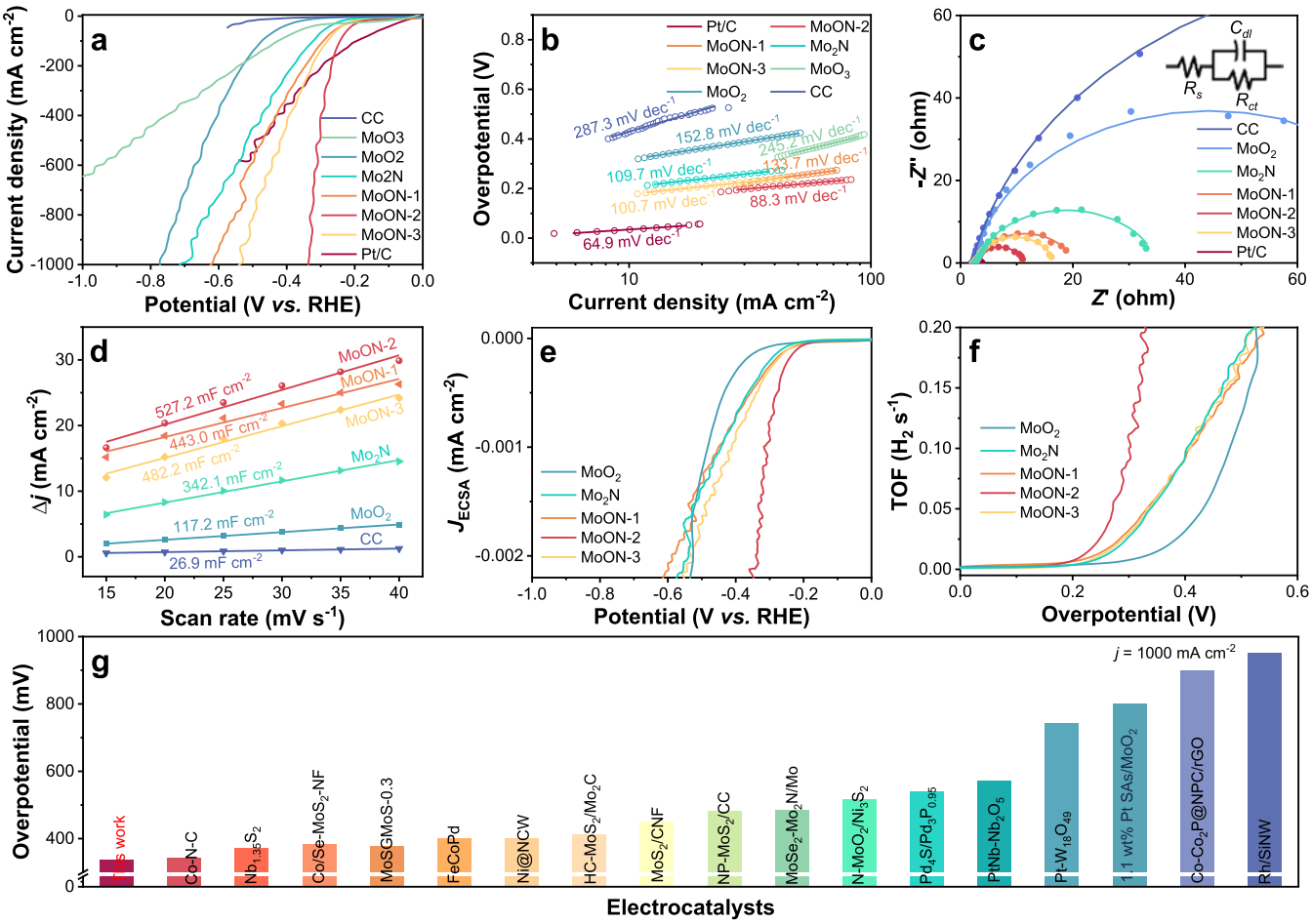

Fig. 4. HER properties of MoO_2, MoON-1, MoON-2, MoON-3, and Mo_2N in 0.5 M H_2SO_4. (a) LSV curves; (b) Tafel plots; (c) EIS; (d) ECSA; (e) LSV based on the ECSA; (f) TOF; (g) Comparison of the overpotentials of the electrocatalyst at 1000 mA cm^{-2} with those of other state-of-the-art electrocatalysts in 0.5 M H_2SO_4.

Fig. S7. Fig. 4**d** shows that MoON-2 has the largest C_{dl} of 527.2 mF cm^{-2}, which is 4.5 times, 1.2 times, 1.1 times, 1.5 times, and 19.6 times larger than those of MoO_2 (117.2 mF cm^{-2}), MoON-1 (443.0 mF cm^{-2}), MoON-3 (482.2 mF cm^{-2}), Mo_2N (342.1 mF cm^{-2}), and CC (26.9 mF cm^{-2}), respectively. The larger ECSA of MoON series electrocatalysts is the result of the heterostructure between the MoO_2 and Mo_2N phases for better activation of the surface sites. A larger C_{dl} implies more electrochemically active site exposure and accelerated HER. The electrocatalytic activity based on the ECSA is analyzed and shown in Fig. 4**e**. The intrinsic electrocatalytic activity of the MoON series electrocatalysts is superior to those of the pure phases of MoO_2/CC and Mo_2N/CC regardless of the ECSA because the interactions between the Mo-O and Mo-N species at the heterointerface promote the HER activity intrinsically. All in all, MoON-2 shows the best HER efficiency, demonstrating that a precisely modulated Mo-O/Mo-N configuration at the MoO_2/-Mo_2N heterointerface optimizes hydrogen adsorption in HER.

The turnover frequency (TOF) stands as a crucial benchmark for assessing the intrinsic activity of HER electrocatalysts. It is defined as the rate of conversion per active site in HER within a unit of time, ultimately determining the intrinsic activity of the electrocatalysts. The utilization of TOF effectively eliminates the comparability issues in catalytic activity stemming from varying catalyst loadings [40–42]. Therefore, TOF is studied to evaluate the intrinsic electrocatalytic capability of the Mo-based electrocatalysts (Supporting note). MoON-2 shows a bigger TOF of 0.20 s^{-1} at an overpotential of 272 mV than the other electrocatalysts, confirming the excellent intrinsic electrocatalytic activity (Fig. 4**f**). The atomic interaction at the heterointerface would be beneficial to the modified electronic structure of the active sites and optimized hydrogen adsorption properties, as a result enhancing the intrinsic catalytic capability of the active sites [30–32]. Fig. 4**g** illustrates the comparison of the overpotentials required for the current density of 1 A cm^{-2} with those of previously reported electrocatalysts including Co-N-C (343 mV) [43], $Nb_{1.35}S_2$ (370 mV) [44], Co/Se--MoS_2-NF (382 mV) [45], MoSGMoS-0.3 (378 mV) [46], FeCoPd (400 mV) [47], Ni@NCW (401 mV) [48], HC-MoS_2/Mo_2C (412 mV) [49], MoS_2/CNF (450 mV) [50], NP-MoS_2/CC (480 mV) [51], $MoSe_2$--Mo_2N/Mo (485 mV) [52], N-MoO_2/Ni_3S_2 (517 mV) [53], Pd_4S/$Pd_3P_{0.95}$ (538 mV) [54], PtNb-Nb_2O_5 (570 mV) [55], Pt-$W_{18}O_{49}$ (743 mV) [56], 1.1 wt% Pt SAs/MoO_2 (800 mV) [57], Co-Co_2P @ NPC/rGO (900 mV) [58], Rh/Si (950 mV) [59]. The results indicate that MoON-2 delivers excellent performance in large current density HER.

Fig. 5**a** shows the high durability of the MoON-2 electrocatalyst at a current density of 1 A cm^{-2} in 0.5 M H_2SO_4 for 180 hours and the LSV curves of MoON-2 before and after the durability test are nearly the same (Fig. 5**b**). In addition, the morphology of MoON-2 is intact with nanowire array structure (Fig. S8), indicating the stable geometrical structure of the as-prepared electrocatalyst during the large current density HER. Fig. S9 shows similar diffraction patterns from the MoON-2 electrocatalyst before and after the long-time test. The XPS spectra of the electrocatalyst after the long-term test in Fig. S10 show similar spectra compared to the pristine sample with a concentration of Mo^{4+}-O and Mo-N species of 44% and 35%, respectively, confirming the excellent stability of the surface chemistry of the electrocatalyst. The hydrogen production rate and Faradaic Efficiency (*FE*) of the MoON-2

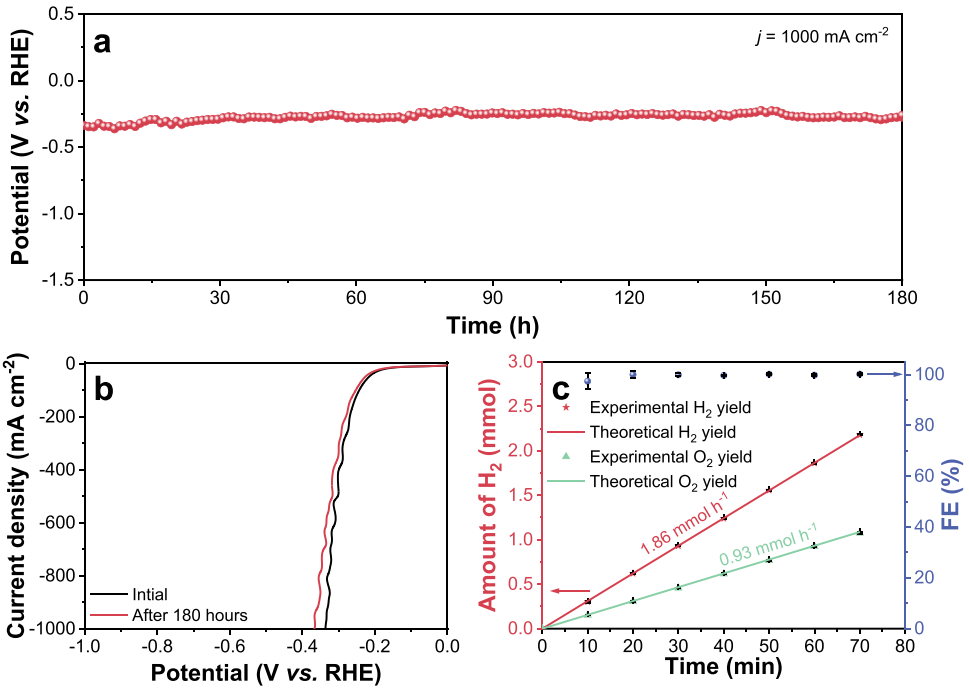

Fig. 5. (a) Stability test of MoON-2; (b) LSV curves of MoON-2 before and after the stability test; (c) Experimental and theoretical amounts of H_2 and O_2 produced by MoON-2 and counter electrode, and *FE* at a current of 100 mA.

electrocatalyst are determined by the water displacement method schematically illustrated in Fig. S11. 53.0 mL of hydrogen and 26.5 mL of oxygen are produced by HER and OER, respectively for 70 min at a constant current of 100 mA. The high-purity H_2 is released from the acidic solution at a rate of 1.86 mmol h^{-1} ((Fig. 5**c**) and *FE* is calculated to be as high as 99.8%.

3.3. DFT calculations

DFT calculations are conducted to elucidate the catalytic mechanism of the as-prepared electrocatalysts. MoO_2 (200) (Fig. S12a) and Mo_2N (200) (Fig. S12b) are adopted to construct the heterointerface between MoO_2 and Mo_2N phases (Fig. S12c) according to the XRD, TEM and HR-TEM results. At the pure MoO_2 (200) surface, the length of the Mo-O bond is in the range of 1.89 ~ 2.05 Å (Fig. S13a) and at the pure Mo_2N (200) surface, the Mo-N bond length is 2.15 ~ 2.23 Å, as shown in Fig. S13b. In the MoO_2(200)/Mo_2N(200) heterostructure, the bond lengths of the Mo-O bond (2.12 ~ 2.16 Å) and Mo-N bond (2.26 Å) are longer than the Mo-O and Mo-N bond lengths, as shown in Fig. S13c. The results reveal that the changes in the bond length of Mo-O and Mo-N in the MoO_2/Mo_2N heterointerface modulate the electronic structure of Mo sites at the MoO_2/Mo_2N heterointerface, demonstrating the interactions between MoO_2 and Mo_2N.

Generally, a ΔG_{H^*} close to 0 eV is preferred for HER [60]. Hydrogen can adsorb on the Mo site of the pure phase of MoO_2 (H-MoO_2) and Mo_2N (H-Mo_2N) as well as the Mo site of Mo_2N phase (H-Mo(Mo_2N)) and MoO_2 phase (H-Mo(MoO_2)) at the MoO_2/Mo_2N heterointerface, as indicated in Fig. 6**a-d** and S14. Fig. 6**e** reveals that the $|\Delta G_{H^*}|$ value of the H-Mo(Mo_2N) site at the MoO_2/Mo_2N heterointerface is only 0.041 eV, which is closer to zero than that of H-Mo(MoO_2) site of 0.080 eV, suggesting that the Mo(Mo_2N) sites at the MoO_2/Mo_2N heterointerface are the active centers in HER. Moreover, the $|\Delta G_{H^*}|$ values of both the H-Mo(Mo_2N) site and H-Mo(MoO_2) site are smaller than those of the pure H-Mo_2N (0.115 eV) and pure H-MoO_2 (0.207 eV), implying that the MoO_2/Mo_2N heterointerface reduces the Mo-H binding and accelerates the release of hydrogen for faster kinetics. The band structure of the electrocatalysts in Fig. S15 indicates that the pure MoO_2, Mo_2N, and MoO_2/Mo_2N heterointerface have a metallic nature. These results indicate that hydrogen adsorption capability on the Mo-based electrocatalysts can be optimized by modulating the Mo-O/Mo-N configuration at the MoO_2/Mo_2N heterointerface.

4. Conclusions

Heterostructured MoO_2/Mo_2N electrocatalysts with tunable Mo-O/Mo-N configurations are synthesized by a programmed nitridation process in ammonia with MoO_3 as the precursor. By precisely controlling the Mo-O and Mo-N contents in the heterostructure, the optimized Mo-O/Mo-N configuration shows weakened hydrogen adsorption characteristics as well as promoted HER kinetics. The MoO_2/Mo_2N electrocatalyst requires an overpotential of only 335 mV for an industrial-scale current density of 1 A cm^{-2} together with a Tafel slope of 88 mV dec^{-1} in 0.5 M H_2SO_4. In addition, the electrocatalyst exhibits excellent stability for 180 hours at a current density of 1 A cm^{-2} with an impressive Faradaic efficiency of 99.8% in HER. The MoO_2/Mo_2N heterostructure with the optimized Mo-O/Mo-N configuration has enormous potential in industrial applications. The results also provide valuable insights into the design and precise modulation of the electronic configurations of low-cost transition metal-based electrocatalysts for industrial-scale hydrogen production.

CRediT authorship contribution statement

Shuai Feng: Methodology, Investigation, Roles/Writing – original draft, Visualization. **Donglian Li:** Methodology, Investigation, Roles/Writing – original draft, Visualization. **Hao Dong:** Investigation, Data curation, Visualization. **Song Xie:** Investigation, Formal analysis, Visualization. **Yaping Miao:** Software, Visualization. **Xuming Zhang:** Methodology, Funding acquisition, Visualization. **Biao Gao:** Methodology, Visualization. **Paul K. Chu:** Funding acquisition, Writing – review & editing, Visualization. **Xiang Peng:** Conceptualization, Funding acquisition, Supervision, Writing – review & editing, Visualization, Project administration.

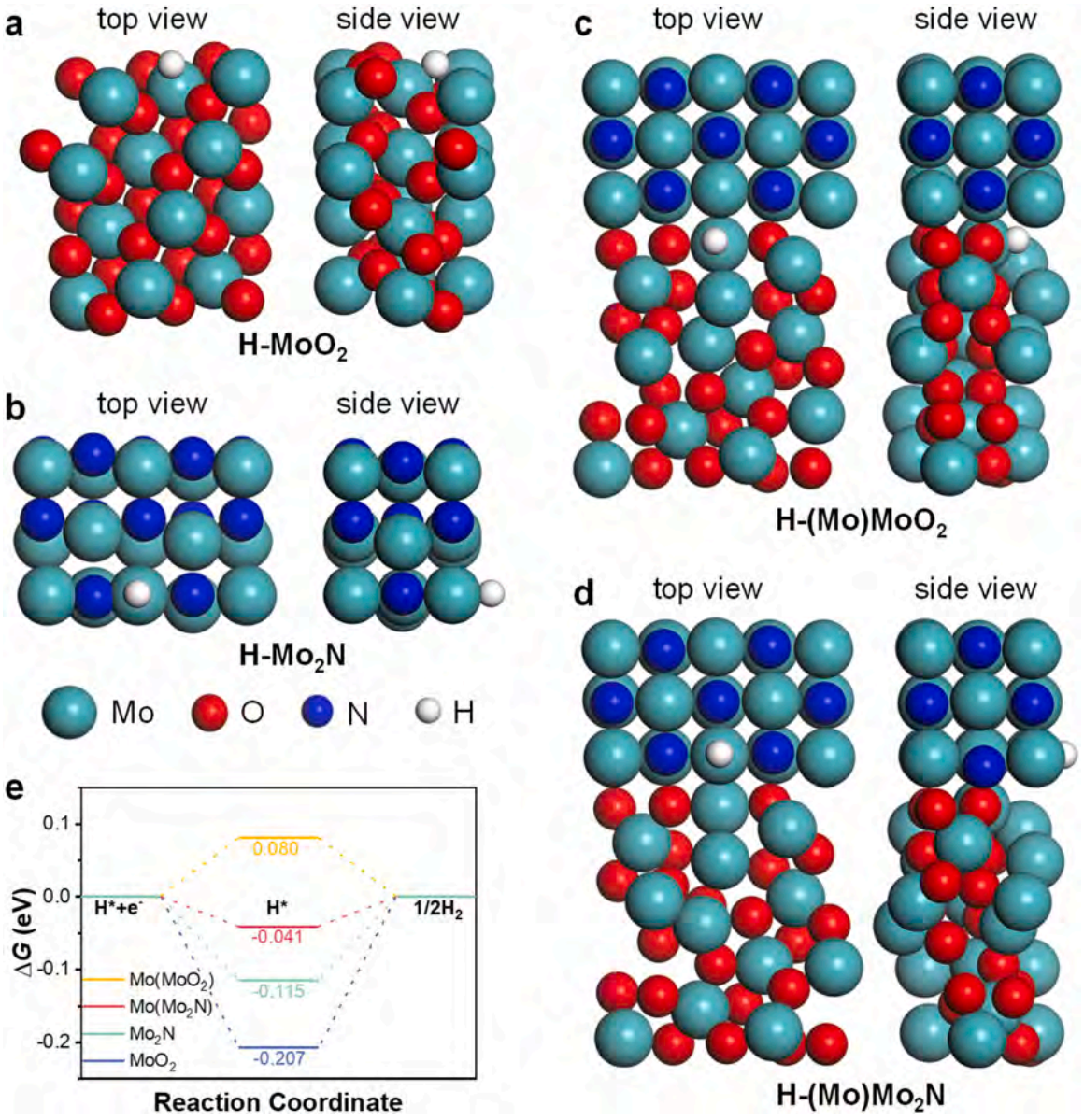

Fig. 6. Optimized surface structures of (a) H-MoO_2, (b) H-Mo_2N, (c) H-Mo(MoO_2), and (d) H-Mo(Mo_2N); (e) Gibbs free energy diagram of MoO_2, Mo_2N, and MoO_2/Mo_2N.

Declaration of Competing Interest

The authors declare that they have no known competing financial interests or personal relationships that could have appeared to influence the work reported in this paper.

Data Availability

Data will be made available on request.

Acknowledgments

This work was financially supported by the National Natural Science Foundation of China (52002294, 22379116), Key Research and Development Program of Hubei Province (2021BAA208), Knowledge Innovation Program of Wuhan-Shuguang Project (2022010801020364), City University of Hong Kong Donation Research Grants (DON-RMG 9229021 and 9220061), as well as City University of Hong Kong Strategic Research Grant (SRG) (7005505).

Appendix A. Supporting information

Supplementary data associated with this article can be found in the online version at doi:10.1016/j.apcatb.2023.123451.

References

[1] H. Ding, H. Liu, W. Chu, C. Wu, Y. Xie, Structural transformation of heterogeneous materials for electrocatalytic oxygen evolution reaction, Chem. Rev. 121 (2021) 13174–13212.
[2] X. Peng, C. Pi, X. Zhang, S. Li, K. Huo, P.K. Chu, Recent progress of transition metal nitrides for efficient electrocatalytic water splitting, Sustain. Energ. Fuels 3 (2019) 366–381.
[3] D. Yan, C. Mebrahtu, S. Wang, R. Palkovits, Innovative electrochemical strategies for hydrogen production: from electricity input to electricity output, Angew. Chem. Int. Ed. 62 (2023), e202214333.
[4] J.-P. Sun, Z. Zhao, J. Li, Z.Z. Li, X.-C. Meng, Recent advances in electrocatalytic seawater splitting, Rare Metals 42 (2023) 751–768.
[5] P. Aggarwal, D. Sarkar, K. Awasthi, P.W. Menezes, Functional role of single-atom catalysts in electrocatalytic hydrogen evolution: Current developments and future challenges, Coord. Chem. Rev. 452 (2022), 214289.

[6] F. Zhou, Y. Zhou, G.G. Liu, C.T. Wang, J. Wang, Recent advances in nanostructured electrocatalysts for hydrogen evolution reaction, Rare Metals 40 (2021) 3375–3405.

[7] X. Wang, H. Yao, C. Zhang, C. Li, K. Tong, M. Gu, Z. Cao, M. Huang, H. Jiang, Double-tuned RuCo dual metal single atoms and nanoalloy with synchronously expedited volmer/tafel kinetics for effective and ultrastable ampere-level current density hydrogen production, Adv. Funct. Mater. 33 (2023), 2301804.

[8] K. Wang, S. Wang, K.S. Hui, J. Li, C. Zha, D.A. Dinh, Z. Shao, B. Yan, Z. Tang, K. N. Hui, Dense platinum/nickel oxide heterointerfaces with abundant oxygen vacancies enable ampere-level current density ultrastable hydrogen evolution in alkaline, Adv. Funct. Mater. 33 (2022), 2211273.

[9] L. Wang, Y. Liu, Z. Chen, Q. Dai, C.-L. Dong, B. Yang, Z. Li, X. Hu, L. Lei, Y. Hou, Theory-guided design of electron-deficient ruthenium cluster for ampere-level current density electrochemical hydrogen evolution, Nano Energy 115 (2023), 108694.

[10] T. Wu, M.-Z. Sun, B.-L. Huang, Non-noble metal-based bifunctional electrocatalysts for hydrogen production, Rare Metals 41 (2022) 2169–2183.

[11] H.Q. Fu, M. Zhou, P.F. Liu, P. Liu, H. Yin, K.Z. Sun, H.G. Yang, M. Al-Mamun, P. Hu, H.-F. Wang, H. Zhao, Hydrogen spillover-bridged Volmer/Tafel processes enabling ampere-level current density alkaline hydrogen evolution reaction under low overpotential, J. Am. Chem. Soc. 144 (2022) 6028–6039.

[12] Y. Zhang, Z. Li, L. Hou, X. Liu, Thermal shrinkage engineering enables electrocatalysts for stable hydrogen evolution at 2000 mA cm^{-2}, Adv. Funct. Mater. 33 (2023), 2213976.

[13] Y.-Z. Wang, Y.-M. Ding, C.-H. Zhang, B.-W. Xue, N.-W. Li, L. Yu, Formation of hierarchical Co-decorated Mo_2C hollow spheres for enhanced hydrogen evolution, Rare Metals 40 (2021) 2785–2792.

[14] Y. Gu, A. Wu, Y. Jiao, H. Zheng, X. Wang, Y. Xie, L. Wang, C. Tian, H. Fu, Two-dimensional porous molybdenum phosphide/nitride heterojunction nanosheets for pH-universal hydrogen evolution reaction, Angew. Chem. Int. Ed. 60 (2021) 6673–6681.

[15] X. Wang, X. Zhang, Y. Xu, H. Song, X. Min, Z. Tang, C. Pi, J. Li, B. Gao, Y. Zheng, X. Peng, P.K. Chu, K. Huo, Heterojunction Mo-based binary and ternary nitride catalysts with Pt-like activity for the hydrogen evolution reaction, Chem. Eng. J. 470 (2023), 144370.

[16] Y. Zhang, P. Guo, S. Guo, X. Xin, Y. Wang, W. Huang, M. Wang, B. Yang, A. Jorge Sobrido, J.B. Ghasemi, J. Yu, X. Li, Gradient heating epitaxial growth gives well lattice-matched Mo_2C-Mo_2N heterointerfaces that boost both electrocatalytic hydrogen evolution and water vapor splitting, Angew. Chem. Int. Ed. 61 (2022), e202209703.

[17] N. Han, P. Liu, J. Jiang, L. Ai, Z. Shao, S. Liu, Recent advances in nanostructured metal nitrides for water splitting, J. Mater. Chem. A 6 (2018) 19912–19933.

[18] Y. Huang, W. Zhou, W. Kong, L. Chen, X. Lu, H. Cai, Y. Yuan, L. Zhao, Y. Jiang, H. Li, L. Wang, L. Wang, H. Wang, J. Zhang, J. Gu, Z. Fan, Atomically interfacial engineering on molybdenum nitride quantum dots decorated N-doped graphene for high-rate and stable alkaline hydrogen production, Adv. Sci. 9 (2022), 2204949.

[19] X. Zhou, Y. Mo, F. Yu, L. Liao, X. Yong, F. Zhang, D. Li, Q. Zhou, T. Sheng, H. Zhou, Engineering active iron sites on nanoporous bimetal phosphide/nitride heterostructure array enabling robust overall water splitting, Adv. Funct. Mater. 33 (2022), 2209465.

[20] D. Su, X. Zhang, A. Wu, H. Yan, Z. Liu, L. Wang, C. Tian, H. Fu, CoO-Mo_2N hollow heterostructure for high-efficiency electrocatalytic hydrogen evolution reaction, NPG Asia Mater. 11 (2019) 78.

[21] C. Wang, X. Lv, P. Zhou, X. Liang, Z. Wang, Y. Liu, P. Wang, Z. Zheng, Y. Dai, Y. Li, M.H. Whangbo, B. Huang, Molybdenum nitride electrocatalysts for hydrogen evolution more efficient than platinum/carbon: Mo_2N/CeO_2@Nickel foam, ACS Appl. Mater. Interfaces 12 (2020) 29153–29161.

[22] Z. Wang, J. Qu, Y. He, T. Xiong, Z. Huang, F. Wang, M.S. Balogun, Exceptional alkaline hydrogen evolution by molybdenum-oxide-nitride-based electrocatalysts with fast water-dissociation and hydrogen-adsorption kinetics, Mater. Chem. Front. 7 (2023) 2683–2692.

[23] M. Zang, N. Xu, G. Cao, Z. Chen, J. Cui, L. Gan, H. Dai, X. Yang, P. Wang, Cobalt molybdenum oxide derived high-performance electrocatalyst for the hydrogen evolution reaction, ACS Catal. 8 (2018) 5062–5069.

[24] P. Qin, S.-Q. Zhang, K.-K.-L. Yung, Z.-F. Huang, B. Gao, Disclosure of charge storage mechanisms in molybdenum oxide nanobelts with enhanced supercapacitive performance induced by oxygen deficiency, Rare Metals 40 (2021) 2447–2454.

[25] C. Li, H. Jang, M.G. Kim, L. Hou, X. Liu, J. Cho, Ru-incorporated oxygen-vacancy-enriched MoO_2 electrocatalysts for hydrogen evolution reaction, Appl. Catal. B-Environ. 307 (2022), 121204.

[26] B. Delley, An all-electron numerical method for solving the local density functional for polyatomic molecules, J. Chem. Phys. 92 (1990) 508–517.

[27] J.K. Nørskov, T. Bligaard, A. Logadottir, J.R. Kitchin, J.G. Chen, S. Pandelov, U. Stimmingc, Trends in the exchange current for hydrogen evolution, J. Electro. Soc. 152 (2005) J23–J26.

[28] X. Peng, S. Xie, S. Xiong, R. Li, P. Wang, X. Zhang, Z. Liu, L. Hu, B. Gao, P. Kelly, P. K. Chu, Ultralow-voltage hydrogen production and simultaneous Rhodamine B beneficiation in neutral wastewater, J. Energy Chem. 81 (2023) 574–582.

[29] X. Peng, S. Xie, X. Wang, C. Pi, Z. Liu, B. Gao, L. Hu, W. Xiao, P.K. Chu, Energy-saving hydrogen production by the methanol oxidation reaction coupled with the hydrogen evolution reaction co-catalyzed by a phase separation induced heterostructure, J. Mater. Chem. A 10 (2022) 20761–20769.

[30] C. Huang, X. Miao, C. Pi, B. Gao, X. Zhang, P. Qin, K. Huo, X. Peng, P.K. Chu, Mo_2C/VC heterojunction embedded in graphitic carbon network: An advanced electrocatalyst for hydrogen evolution, Nano Energy 60 (2019) 520–526.

[31] X. Peng, Y. Yan, X. Jin, C. Huang, W. Jin, B. Gao, P.K. Chu, Recent advance and prospectives of electrocatalysts based on transition metal selenides for efficient water splitting, Nano Energy 78 (2020), 105234.

[32] L. Xiong, Y. Qiu, X. Peng, Z. Liu, P.K. Chu, Electronic structural engineering of transition metal-based electrocatalysts for the hydrogen evolution reaction, Nano Energy 104 (2022), 107882.

[33] R. Li, S. Xie, Y. Zeng, Q. Zhao, M. Mao, Z. Liu, P.K. Chu, X. Peng, Synergistic dual-regulating the electronic structure of NiMo selenides composite for highly efficient hydrogen evolution reaction, Fuel 358 (2024), 130203.

[34] S. Zhang, Y. Yao, X. Jiao, M. Ma, H. Huang, X. Zhou, L. Wang, J. Bai, Y. Yu, Mo_2N-W_2N heterostructures embedded in spherical carbon superstructure as highly efficient polysulfide electrocatalysts for stable room-temperature Na-S batteries, Adv. Mater. 33 (2021), 2103846.

[35] H.-X. Liu, J.-Y. Li, X. Qin, C. Ma, W.-W. Wang, K. Xu, H. Yan, D. Xiao, C.-J. Jia, Q. Fu, D. Ma, Pt_n-O_v synergistic sites on MoO_x/γ-Mo_2N heterostructure for low-temperature reverse water-gas shift reaction, Nat. Commun. 13 (2022) 5800.

[36] T. Wang, P. Wang, W. Zang, X. Li, D. Chen, Z. Kou, S. Mu, J. Wang, Nanoframes of Co_3O_4-Mo_2N heterointerfaces enable high-performance bifunctionality toward both electrocatalytic HER and OER, Adv. Funct. Mater. 32 (2021), 2107382.

[37] J. Qiu, Z. Yang, Q. Li, Y. Li, X. Wu, C. Qi, Q. Qiao, Formation of N-doped molybdenum carbide confined in hierarchical and hollow carbon nitride microspheres with enhanced sodium storage properties, J. Mater. Chem. A 4 (2016) 13296–13306.

[38] G. Na, X. Chen, R. Zhao, J. Du, Phase engineering of molybdenum carbide/oxide for highly-efficient electrocatalytic hydrogen production, Chem. Asian J. 18 (2023), e202300292.

[39] G.L. Li, X.Y. Qiao, Y.Y. Miao, T.Y. Wang, F. Deng, Synergistic effect of N-$NiMoO_4$/Ni heterogeneous interface with oxygen vacancies in N-$NiMoO_4$/Ni/CNTs for superior overall water splitting, Small 19 (2023), 2207196.

[40] R. Andaveh, A. Sabour Rouhaghdam, J. Ai, M. Maleki, K. Wang, A. Seif, G. Barati Darband, J. Li, Boosting the electrocatalytic activity of NiSe by introducing MnCo as an efficient heterostructured electrocatalyst for large-current-density alkaline seawater splitting, Appl. Catal. B-Environ. 325 (2023), 122355.

[41] Y.-W. Wei, G. Yang, X.-X. Xu, Y.-Y. Liu, N.-X. Kang, B.-J. Li, Y.-Z. Wang, Y.-X. Zhao, Ultrafine Ru nanoparticles anchored on core–shell structured zeolite-carbon for efficient catalysis of hydrogen generation, Rare Metals 42 (2023) 2324–2334.

[42] S. Anantharaj, S. Kundu, Do the evaluation parameters reflect intrinsic activity of electrocatalysts in electrochemical water splitting? ACS Energy Lett. 4 (2019) 1260–1264.

[43] R. Liu, Z. Gong, J. Liu, J. Dong, J. Liao, H. Liu, H. Huang, J. Liu, M. Yan, K. Huang, H. Gong, J. Zhu, C. Cui, G. Ye, H. Fei, Design of aligned porous carbon films with single-atom Co-N-C sites for high-current-density hydrogen generation, Adv. Mater. 33 (2021), 2103533.

[44] J. Yang, A.R. Mohmad, Y. Wang, R. Fullon, X. Song, F. Zhao, I. Bozkurt, M. Augustin, E.J.G. Santos, H.S. Shin, W. Zhang, D. Voiry, H.Y. Jeong, M. Chhowalla, Ultrahigh-current-density niobium disulfide catalysts for hydrogen evolution, Nat. Mater. 18 (2019) 1309–1314.

[45] Z. Zheng, L. Yu, M. Gao, X. Chen, W. Zhou, C. Ma, L. Wu, J. Zhu, X. Meng, J. Hu, Y. Tu, S. Wu, J. Mao, Z. Tian, D. Deng, Boosting hydrogen evolution on MoS_2 *via* co-confining selenium in surface and cobalt in inner layer, Nat. Commun. 11 (2020) 3315.

[46] S.A. Shah, G. Zhu, X. Shen, L. Kong, Z. Ji, K. Xu, H. Zhou, J. Zhu, P. Song, C. Song, A. Yuan, X. Miao, Controllable sandwiching of reduced graphene oxide in hierarchical defect-rich MoS_2 ultrathin nanosheets with expanded interlayer spacing for electrocatalytic hydrogen evolution reaction, Adv. Mater. Interfaces 5 (2018), 1801093.

[47] A. Kumar, S.K. Purkayastha, A.K. Guha, M.R. Das, S. Deka, Robust and promising hydrogen and oxygen evolution reactions by a nanostructured bifunctional FeCoPd Alloy Electrocatalyst, J. Mater. Chem. A 10 (2022) 23731–23743.

[48] D. Li, H. Cheng, X. Hao, G. Yu, C. Qiu, Y. Xiao, H. Huang, Y. Lu, B. Zhang, Wood-derived freestanding carbon-based electrode with hierarchical structure for industrial-level hydrogen production, Adv. Mater. (2023), https://doi.org/10.1002/adma.202304917.

[49] C. Zhang, Y. Luo, J. Tan, Q. Yu, F. Yang, Z. Zhang, L. Yang, H.-M. Cheng, B. Liu, High-throughput production of cheap mineral-based two-dimensional electrocatalysts for high-current-density hydrogen evolution, Nat. Commun. 11 (2020) 3724.

[50] Z. Zhang, Y. Wang, X. Leng, V.H. Crespi, F. Kang, R. Lv, Controllable edge exposure of MoS_2 for efficient hydrogen evolution with high current density, ACS Appl. Energy Mater. 1 (2018) 1268–1275.

[51] K. Sun, L. Zeng, S. Liu, L. Zhao, H. Zhu, J. Zhao, Z. Liu, D. Cao, Y. Hou, Y. Liu, Y. Pan, C. Liu, Design of basal plane active MoS_2 through one-step nitrogen and phosphorus co-doping as an efficient pH-universal electrocatalyst for hydrogen evolution, Nano Energy 58 (2019) 862–869.

[52] C. Jian, W. Hong, Q. Cai, W. Liu, The local electronic structure modulation of the molybdenum selenide-nitride heterojunction for efficient hydrogen evolution reaction, J. Mater. Chem. A 9 (2021) 26113–26118.

[53] L. Wang, J. Cao, C. Lei, Q. Dai, B. Yang, Z. Li, X. Zhang, C. Yuan, L. Lei, Y. Hou, Strongly coupled 3D N-doped MoO_2/Ni_3S_2 hybrid for high current density hydrogen evolution electrocatalysis and biomass upgrading, ACS Appl. Mater. Interfaces 11 (2019) 27743–27750.

[54] G. Zhang, A. Wang, L. Niu, W. Gao, W. Hu, Z. Liu, R. Wang, J. Chen, Interfacial engineering to construct antioxidative Pd_4S/$Pd_3P_{0.95}$ heterostructure for robust

hydrogen production at high current density, Adv. Energy Mater. 12 (2022), 2103511.
[55] N. Nie, D. Zhang, Z. Wang, W. Yu, S. Ge, J. Xiong, Y. Gu, B. Yang, J. Lai, L. Wang, Stable PtNb-Nb_2O_5 heterostructure clusters@CC for high-current-density neutral seawater hydrogen evolution, Appl. Catal. B-Environ. 318 (2022), 121808.
[56] W.X. Li, Z.Y. Liu, S.C. Yang, J.N. Wu, L. Sun, E.G. Ma, H.G. Yang, X. Guo, Highly dispersed Pt species anchored on $W_{18}O_{49}$ nanowires mediate efficient and durable hydrogen evolution in acidic water, Sci. China Mater. 65 (2022) 3435–3441.
[57] Y. Qiu, S. Liu, C. Wei, J. Fan, H. Yao, L. Dai, G. Wang, H. Li, B. Su, X. Guo, Synergistic effect between platinum single atoms and oxygen vacancy in MoO_2 boosting pH-Universal hydrogen evolution reaction at large current density, Chem. Eng. J. 427 (2022), 131309.
[58] G. Li, J. Yu, J. Jia, L. Yang, L. Zhao, W. Zhou, H. Liu, Cobalt-cobalt phosphide nanoparticles@nitrogen-phosphorus doped carbon/graphene derived from cobalt ions adsorbed saccharomycete yeasts as an efficient, stable, and large-current-density electrode for hydrogen evolution reactions, Adv. Funct. Mater. 28 (2018), 1801332.
[59] L. Zhu, H. Lin, Y. Li, F. Liao, Y. Lifshitz, M. Sheng, S.T. Lee, M. Shao, A rhodium/silicon co-electrocatalyst design concept to surpass platinum hydrogen evolution activity at high overpotentials, Nat. Commun. 7 (2016) 12272.
[60] J. Sun, S. Qin, Z. Zhang, C. Li, X. Xu, Z. Li, X. Meng, Joule heating synthesis of well lattice-matched $Co_2Mo_3O_8/MoO_2$ heterointerfaces with greatly improved hydrogen evolution reaction in alkaline seawater electrolysis with 12.4% STH efficiency, Appl. Catal. B-Environ. 338 (2023), 123015.

Supporting information

Tailoring the Mo-N/Mo-O configuration in MoO_2/Mo_2N heterostructure for ampere-level current density hydrogen production

Shuai Feng[1#], Donglian Li[1#], Hao Dong[1], Song Xie[1], Yaping Miao[2], Xuming Zhang[3], Biao Gao[3], Paul K. Chu[4], Xiang Peng[1]*

[1] Hubei Key Laboratory of Plasma Chemistry and Advanced Materials, Engineering Research Center of Phosphorus Resources Development and Utilization of Ministry of Education, School of Materials Science and Engineering, Wuhan Institute of Technology, Wuhan, 430205, China

[2] School of Textile Science and Engineering, Xi'an Polytechnic University, Xi'an, 710048, China

[3] The State Key Laboratory of Refractories and Metallurgy, Institute of Advanced Materials and Nanotechnology, Wuhan University of Science and Technology, Wuhan 430081, China

[4] Department of Physics, Department of Materials Science and Engineering, and Department of Biomedical Engineering, City University of Hong Kong, Tat Chee Avenue, Kowloon, Hong Kong, China

[#] These authors contributed equally to this work.

* Correspondence: xpeng@wit.edu.cn (X. Peng)

Supplementary note: TOF calculation

TOF values are calculated according to the method reported by the Jaramillo group [1]. The detailed process is shown as follows:

To calculate the per-site TOF, we use the following formula:

$$TOF = \frac{number\ of\ total\ hydrogen\ turnovers/cm^2}{number\ of\ active\ of\ sites/cm^2} \qquad (2)$$

The total number of hydrogen turnovers is calculated from the current density according to:

$$No.of\ H_2 = \left(j\frac{mA}{cm^2}\right)\left(\frac{1\ C\ s^{-1}}{1000\ mA}\right)\left(\frac{1\ mol\ e^{-1}}{96485.3\ C}\right)\left(\frac{1\ mol\ H_2}{2\ mol\ e^{-1}}\right)\left(\frac{6.022\times10^{23}H_2\ mulecules}{1\ mol\ H_2}\right)$$

$$= 3.12\times10^{15}\frac{H_2\ s^{-1}}{cm^2}per\frac{mA}{cm^2}$$

The active sites per real surface area are calculated from the following formula:

$$No.of\ active\ sites = \left(\frac{No.of\ atoms/unit\ cell}{Volunme/unit\ cell}\right)^{\frac{2}{3}}$$

Thus, the calculation of the number of active sites of MoO_2-Mo_2N/CC should follow the formula:

$$No.of\ active\ sites \times ECSA$$

$$= \left(\frac{No.of\ atoms/unit\ cell}{Volume/unit\ cell}\right)^{\frac{2}{3}} \times x \times ECSA$$

$$+ \left(\frac{No.of\ atoms/unit\ cell}{Volume/unit\ cell}\right)^{\frac{2}{3}} \times y \times ECSA$$

Where x and y are the molar ratios of MoO_2 and Mo_2N at the surface of MoO_2-Mo_2N electrodes. As it is known that the unit cell of Mo contains two atoms with a volume of 31.1 $Å^3$, MoO_2 contains one Mo atom and two O atoms with a volume of 131.5 $Å^3$ and Mo_2N contains two Mo atoms and one N atom with a volume of 72.2 $Å^3$. For the phase composition ratio of MoO_2 and Mo_2N determined by the XRD phase quantitative analysis using Jade 6.5, we cans estimate that

MoON-1, and MoON-2, contains 90.6% MoO_2 and 9.4% Mo_2N, and 58.2% MoO_2 and 41.8% Mo_2N, respectively.

Thus,

For MoO_2:

$$No.of\ active\ sites = \left(\frac{No.of\ atoms/unit\ cell}{Volunme/unit\ cell}\right)^{\frac{2}{3}}$$

$$No.of\ active\ sites = \left(\frac{3\ atoms/unit\ cell}{131.5\ \text{Å}^3/unit\ cell}\right)^{\frac{2}{3}}$$

No. of active sites = 5.577×10^{14} atoms cm^{-2}

$$ECSA = \frac{Specific\ capacitance\ (\mu F\ cm^{-2})}{40\ \mu F\ cm^{-2}\ per\ cm^2_{ECSA}} = A_{geo} \times \frac{117200\ (\mu F\ cm^{-2})}{40\ \mu F\ cm^{-2}}$$

$$TOF = \frac{(3.12 \times 10^{15}\ \frac{H_2\ s^{-1}}{cm^2}\ per\ \frac{mA}{cm^2}) \times |j|}{no.of\ active\ sites\ \times ECSA}$$

For MoON-1:

$$No.of\ active\ sites = \left(\frac{No.of\ atoms/unit\ cell}{Volunme/unit\ cell}\right)^{\frac{2}{3}}$$

$$No.of\ active\ sites\ (\mathrm{MoO_2}) = \left(\frac{3\ atoms/unit\ cell}{131.5\ \text{Å}^3/unit\ cell}\right)^{\frac{2}{3}}$$

No. of active sites (MoO_2) = 5.577×10^{14} atoms cm^{-2}

$$No.of\ active\ sites\ (\mathrm{Mo_2N}) = \left(\frac{3\ atoms/unit\ cell}{72.2\ \text{Å}^3/unit\ cell}\right)^{\frac{2}{3}}$$

No. of active sites (Mo_2N) = 8.318×10^{14}atoms cm^{-2}

$$ECSA = \frac{Specific\ capacitance\ (\mu F\ cm^{-2})}{40\ \mu F\ cm^{-2}\ per\ cm^2_{ECSA}} = A_{geo} \times \frac{443000\ (\mu F\ cm^{-2})}{40\ \mu F\ cm^{-2}}$$

$$TOF = \frac{(3.12 \times 10^{15} \frac{H_2\ s^{-1}}{cm^2} per \frac{mA}{cm^2}) \times |j|}{no.of\ active\ sites\ (MoO_2) \times x \times ECSA + no.of\ active\ sites\ (Mo_2N) \times y \times ECSA}$$

Where x = 90.6% and y = 9.4%.

For MoON-2:

$$No.of\ active\ sites = \left(\frac{No.of\ atoms/unit\ cell}{Volunme/unit\ cell}\right)^{\frac{2}{3}}$$

$$No.of\ active\ sites\ (\mathrm{MoO_2}) = \left(\frac{3\ atoms/unit\ cell}{131.5\ Å^3/unit\ cell}\right)^{\frac{2}{3}}$$

No. of active sites (MoO_2) = 5.577×10^{14} atoms cm^{-2}

$$No.of\ active\ sites\ (\mathrm{Mo_2N}) = \left(\frac{3\ atoms/unit\ cell}{72.2\ Å^3/unit\ cell}\right)^{\frac{2}{3}}$$

No. of active sites (Mo_2N) = 8.318×10^{14}atoms cm^{-2}

$$ECSA = \frac{Specific\ capacitance\ (\mu F\ cm^{-2})}{40\ \mu F\ cm^{-2}\ per\ cm^2_{ECSA}} = A_{geo} \times \frac{527200\ (\mu F\ cm^{-2})}{40\ \mu F\ cm^{-2}}$$

$$TOF = \frac{(3.12 \times 10^{15} \frac{H_2\ s^{-1}}{cm^2} per \frac{mA}{cm^2}) \times |j|}{no.of\ active\ sites\ (MoO_2) \times x \times ECSA + no.of\ active\ sites\ (Mo_2N) \times y \times ECSA}$$

Where x = 58.2% and y = 41.8%.

For MoON-3:

$$No.of\ active\ sites\ (\mathrm{Mo_2N}) = \left(\frac{3\ atoms/unit\ cell}{72.2\ Å^3/unit\ cell}\right)^{\frac{2}{3}}$$

No. of active sites (Mo_2N) = 8.318×10^{14}atoms cm^{-2}

$$ECSA = \frac{Specific\ capacitance\ (\mu F\ cm^{-2})}{40\ \mu F\ cm^{-2}\ per\ cm^2_{ECSA}} = A_{geo} \times \frac{482200\ (\mu F\ cm^{-2})}{40\ \mu F\ cm^{-2}}$$

$$TOF = \frac{(3.12 \times 10^{15} \frac{H_2\ s^{-1}}{cm^2} per \frac{mA}{cm^2}) \times |j|}{no.of\ active\ sites\ (Mo_2N) \times ECSA}$$

For Mo_2N:

$$No.of\ active\ sites = \left(\frac{No.of\ atoms/unit\ cell}{Volumme/unit\ cell}\right)^{\frac{2}{3}}$$

$$No.of\ active\ sites\ (\mathrm{Mo_2N}) = \left(\frac{3\ atoms/unit\ cell}{72.2\ \text{Å}^3/unit\ cell}\right)^{\frac{2}{3}}$$

No. of active sites (Mo_2N) = 8.318×10^{14} atoms cm^{-2}

$$ECSA = \frac{Specific\ capacitance\ (\mu F\ cm^{-2})}{40\ \mu F\ cm^{-2}\ per\ cm^2_{ECSA}} = A_{geo} \times \frac{342100\ (\mu F\ cm^{-2})}{40\ \mu F\ cm^{-2}}$$

$$TOF = \frac{(3.12 \times 10^{15} \frac{H_2\ s^{-1}}{cm^2} per \frac{mA}{cm^2}) \times |j|}{no.of\ active\ sites\ (Mo_2N) \times ECSA}$$

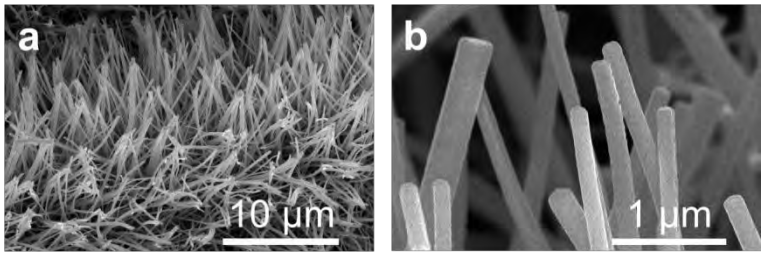

Figure S1. SEM image of MoON-1

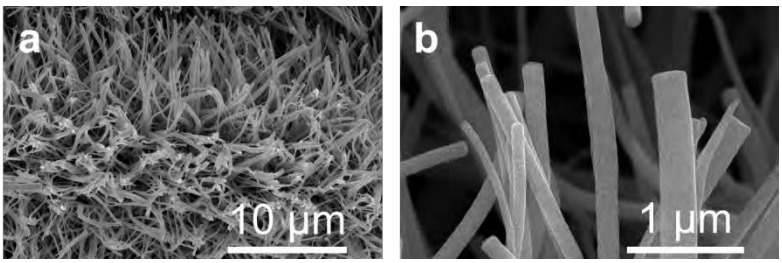

Figure S2. SEM image of MoON-3

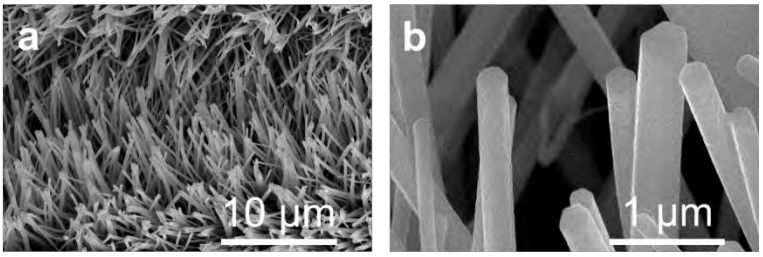

Figure S3. SEM of MoO_2/CC

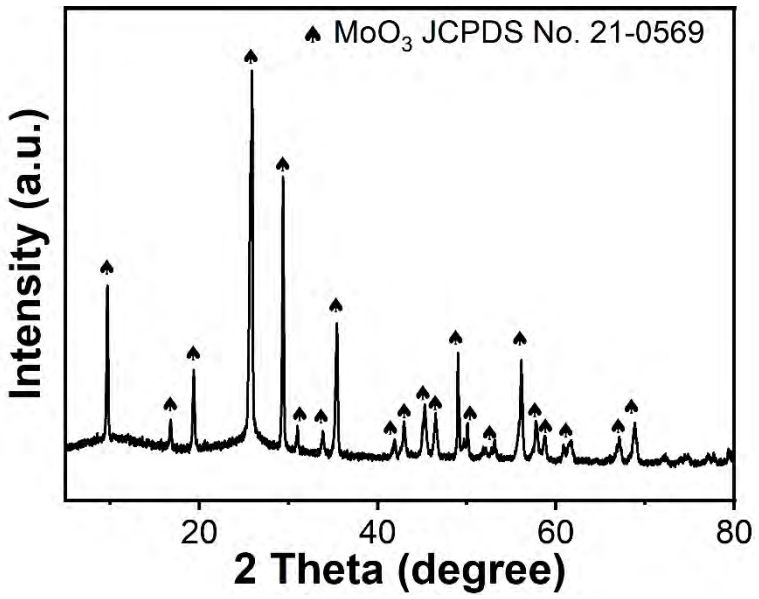

Figure S4. XRD of MoO_3/CC.

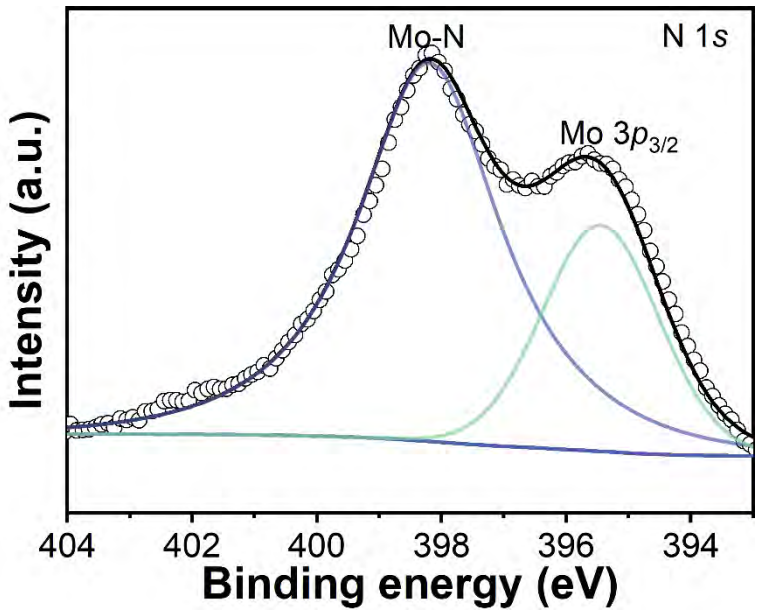

Figure S5. High-resolution XPS N-1s spectra of the MoON-2.

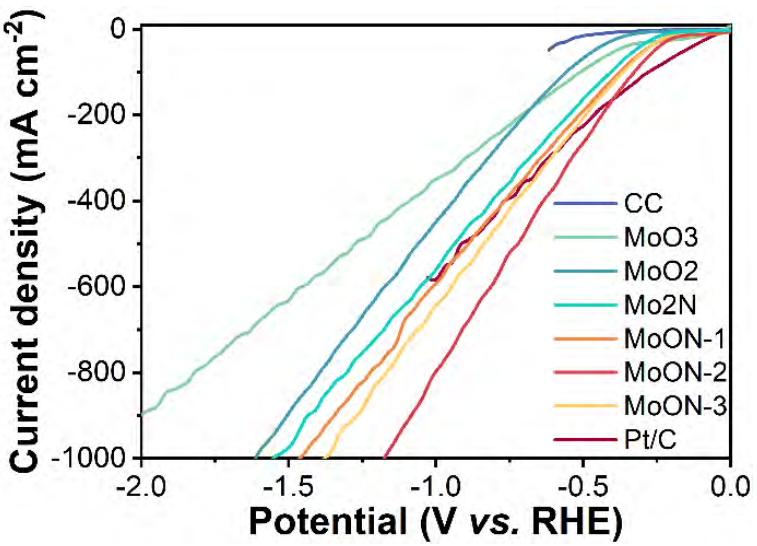

Figure S6. The LSV curves of MoO_3, MoO_2, MoON-1, MoON-2, MoON-3, Mo_2N, Pt/C, and CC without *iR*-correction.

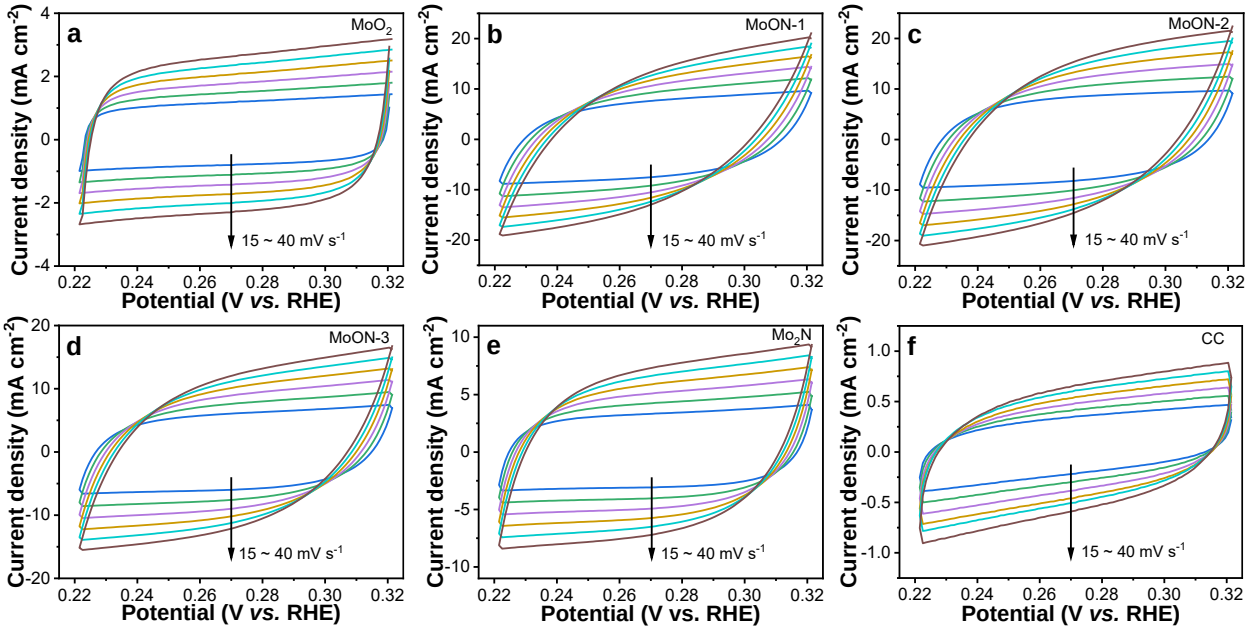

Figure S7. CV for ECSA.

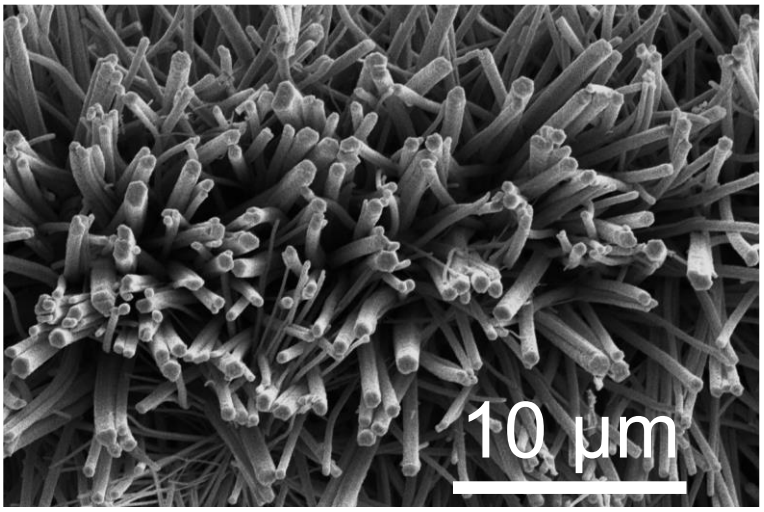

Figure S8. SEM of the MoON-2 electrocatalyst after the long-term test.

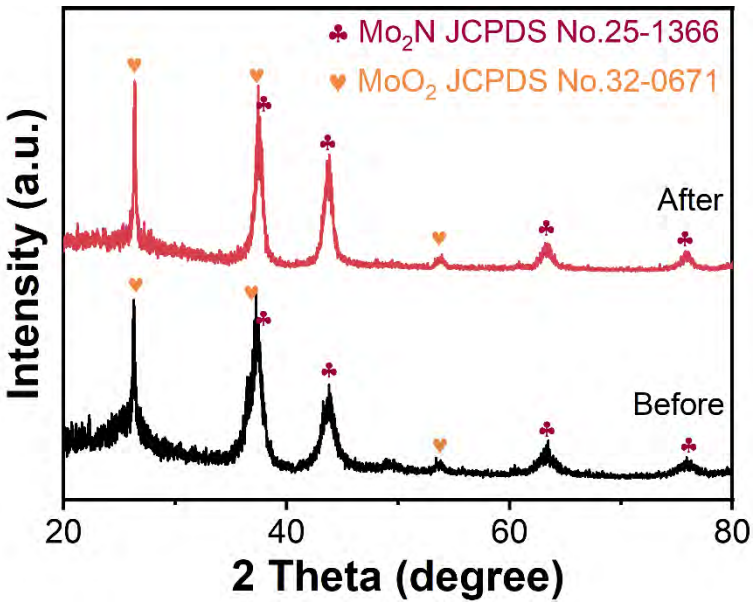

Figure S9. XRD patterns of the MoON-2 before and after long-term stability test.

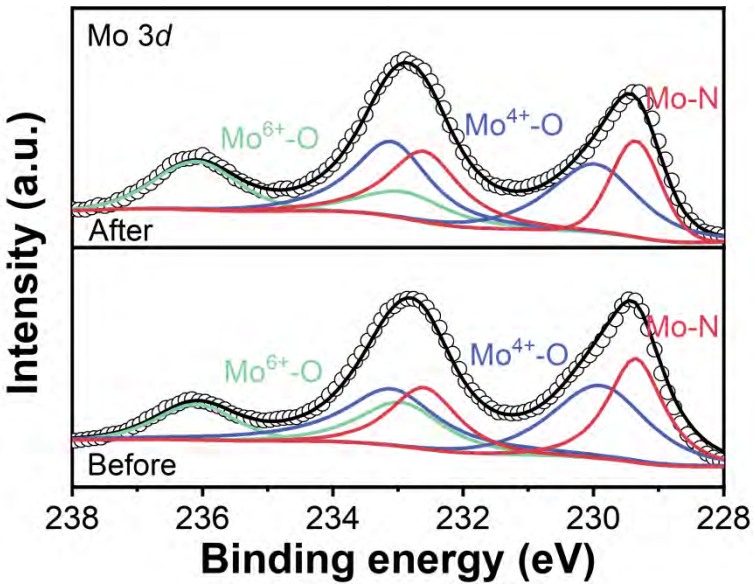

Figure S10. High-resolution XPS Mo-3*d* of the MoON-2 electrocatalyst before and after the long-term test.

Figure S11. Photograph of the water splitting system with the MoON-2 electrocatalyst and O_2 (left) and H_2 (right) gas generation determined by the water displacement method.

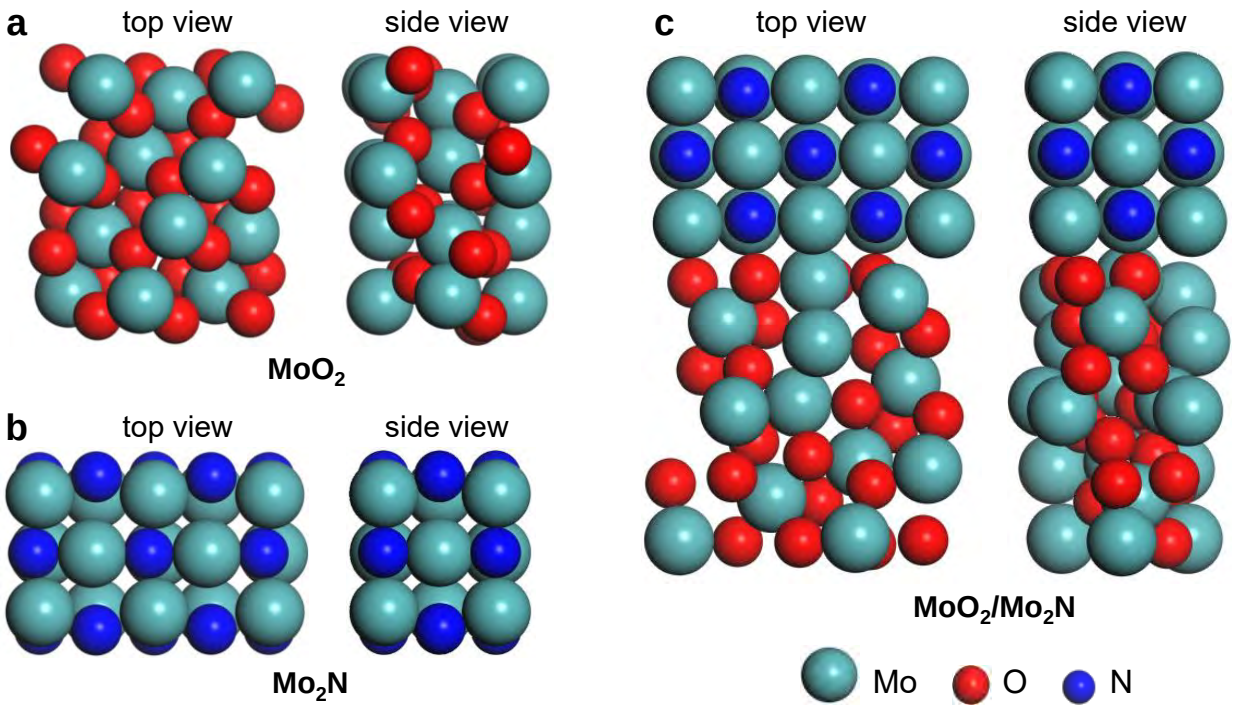

Figure S12. The top and side view of (a) MoO_2, (b) Mo_2N, (c) MoO_2/Mo_2N.

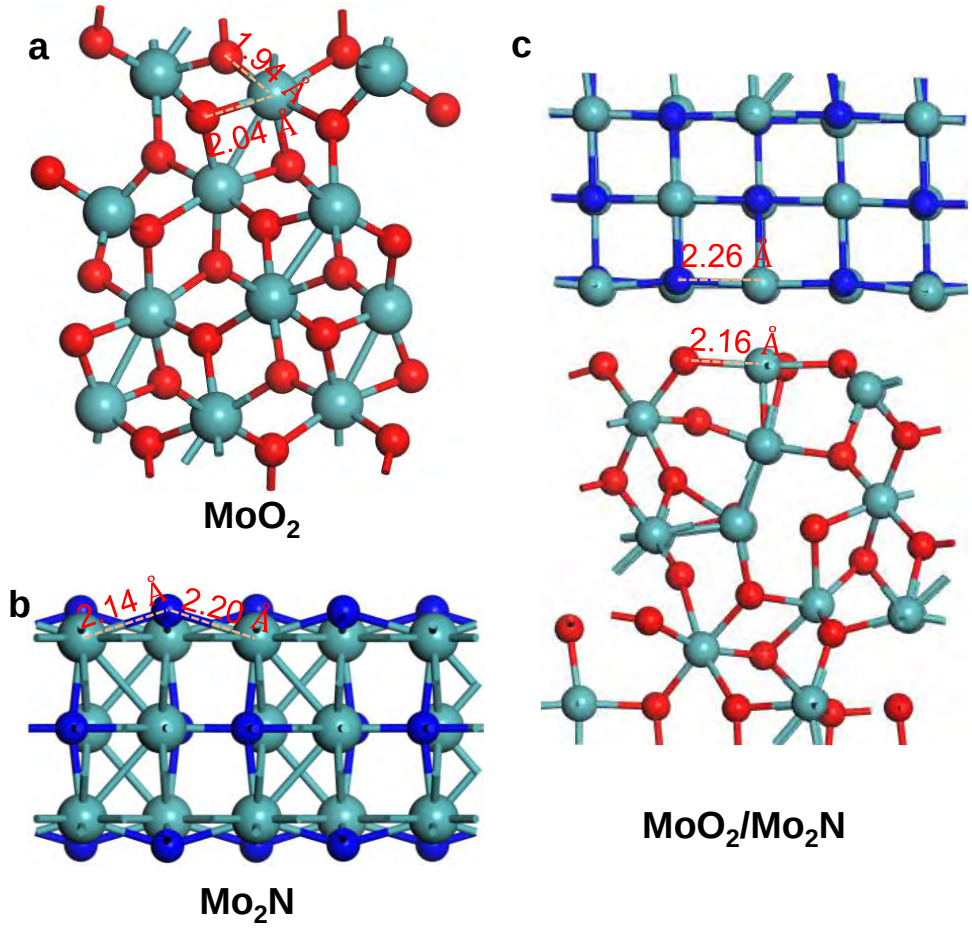

Figure S13. The bond lengths of M-X (M = Mo, X = N, O) bonds in (a) MoO_2, (b) Mo_2N, and (c) MoO_2/Mo_2N heterostructure.

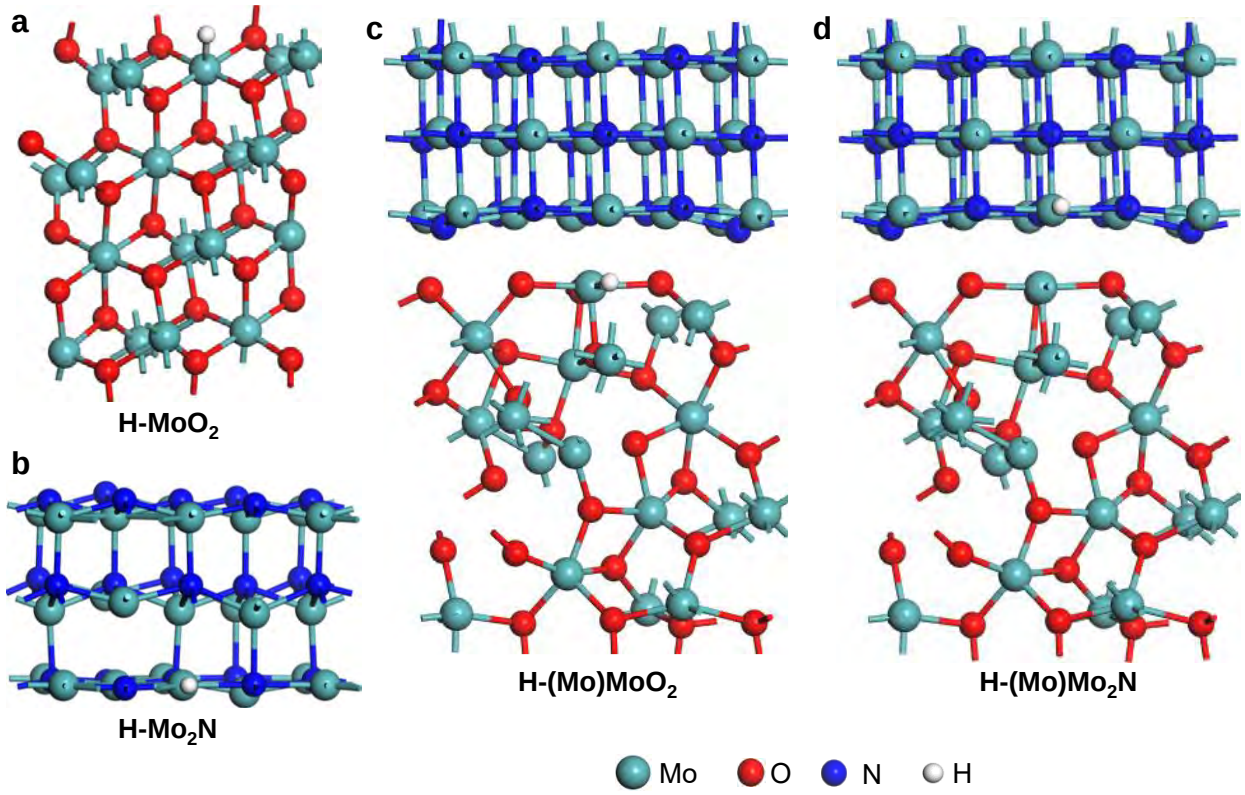

Figure S14. The simulated models of (a) H-MoO_2, (b) H-Mo_2N, (c) H-(Mo)MoO_2, and (d) H-(Mo)Mo_2N.

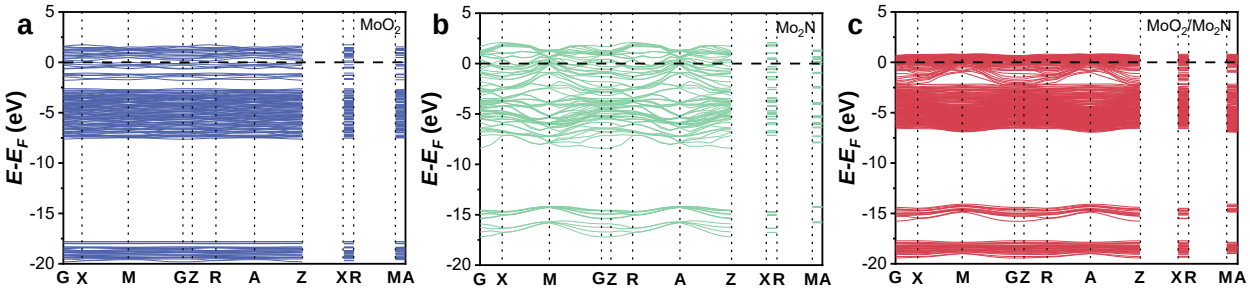

Figure S15. The band structures of (a) MoO_2, (b) Mo_2N, and (c) MoO_2/Mo_2N heterostructure.

References

[1] J. Kibsgaard, T.F. Jaramillo, Molybdenum phosphosulfide: an active, acid-stable, earth-abundant catalyst for the hydrogen evolution reaction, Angew. Chem. Int. Ed., 53 (2014) 14433-14437.